The Journal of Chemical Physics

Magnetic quantification of single-crystalline Fe and Co nanowires via off-axis electron holography

Cite as: J. Chem. Phys. **152**, 114202 (2020); https://doi.org/10.1063/1.5145337
Submitted: 16 January 2020 . Accepted: 05 March 2020 . Published Online: 20 March 2020

Ke Chai, Zi-An Li, Wenting Huang, Gunther Richter, Ruibin Liu, Bingsuo Zou, Jan Caron, András Kovács, Rafal E. Dunin-Borkowski, and Jianqi Li

View Online Export Citation CrossMark

ARTICLES YOU MAY BE INTERESTED IN

Structure of two-dimensional Fe_3O_4
The Journal of Chemical Physics **152**, 114705 (2020); https://doi.org/10.1063/1.5142558

A novel multiscale scheme to accelerate atomistic simulations of bio-macromolecules by adaptively driving coarse-grained coordinates
The Journal of Chemical Physics **152**, 114115 (2020); https://doi.org/10.1063/1.5135309

Energetics and mechanisms for the acetonyl radical + O_2 reaction: An important system for atmospheric and combustion chemistry
The Journal of Chemical Physics **152**, 114301 (2020); https://doi.org/10.1063/1.5141859

J. Chem. Phys. **152**, 114202 (2020); https://doi.org/10.1063/1.5145337 **152**, 114202

AIP Publishing

Magnetic quantification of single-crystalline Fe and Co nanowires via off-axis electron holography

Cite as: J. Chem. Phys. **152**, 114202 (2020); doi: 10.1063/1.5145337
Submitted: 16 January 2020 • Accepted: 5 March 2020 •
Published Online: 20 March 2020

Ke Chai,[1,2] Zi-An Li,[2,a)] Wenting Huang,[3] Gunther Richter,[3] Ruibin Liu,[1,b)] Bingsuo Zou,[1,c)]
Jan Caron,[4] András Kovács,[4] Rafal E. Dunin-Borkowski,[4] and Jianqi Li[2]

AFFILIATIONS

[1] Beijing Key Laboratory of Nano Photonics and Ultrafine Optoelectronic Systems, School of Physics, Beijing Institute of Technology, Beijing 100081, People's Republic of China

[2] Beijing National Laboratory for Condensed Matter Physics and Institute of Physics, Chinese Academy of Sciences, Beijing 100190, People's Republic of China

[3] Max Planck Institute for Intelligent Systems, Heisenbergstrasse 3, D-70569 Stuttgart, Germany

[4] Ernst Ruska-Centre for Microscopy and Spectroscopy with Electrons and Peter Grünberg Institute, Forschungszentrum Jülich, D-52425 Jülich, Germany

[a)] **Author to whom correspondence should be addressed:** zali79@iphy.ac.cn
[b)] liuruibin8@gmail.com
[c)] zoubs@bit.edu.cn

ABSTRACT

Investigating the local micromagnetic structure of ferromagnetic nanowires (NWs) at the nanoscale is essential to study the structure–property relationships and can facilitate the design of nanostructures for technology applications. Herein, we synthesized high-quality iron and cobalt NWs and investigated the magnetic properties of these NWs using off-axis electron holography. The Fe NWs are about 100 nm in width and a few micrometers in length with a preferential growth direction of [100], while the Co NWs have a higher aspect-ratio with preferential crystal growth along the [110] direction. It is noted that compact passivation surface layers of oxides protect these NWs from further oxidation, even after nearly two years of exposure to ambient conditions; furthermore, these NWs display homogeneous ferromagnetism along their axial direction revealing the domination of shape anisotropy on magnetic behavior. Importantly, the average value of magnetic induction strengths of Fe NWs (2.07 {±} 0.10 T) and Co NWs (1.83 {±} 0.15 T) is measured to be very close to the respective theoretical value, and it shows that the surface oxide layers do not affect the magnetic moments in NWs. Our results provide a useful synthesis approach for the fabrication of single-crystalline, defect-free metal NWs and give insight into the micromagnetic properties in ferromagnetic NWs based on the transmission electron microscopy measurements.

INTRODUCTION

Owing to their novel magnetic properties that arise from the unique one-dimensional (1D) structure, there have been intense research interests in ferromagnetic NWs from both academic and applied perspectives for the last few decades.[1–6] Some of the intrinsically magnetic NWs with high aspect-ratio show great potential at miniaturized magnetic sensors, such as the Magnetic Force Microscope (MFM) probe, for it contributes to enhancing the resolution of imaging.[7,8] To realize these applications, the very first step is to fabricate high-quality magnetic NWs structures. In this regard, several fabrication routes, including wet-chemistry,[6,9,10] electrochemical deposition (ECD) with porous alumina templates,[11–13] chemical and physical vapor depositions (CVD[14–18] and PVD[19,20]), and focused electron-beam-induced deposition (FEBID),[21,22] have been established to obtain various types of 1D magnetic structures. Generally, most of the magnetic NWs fabricated via ECD and FEBID techniques are found to be polycrystalline with various grain sizes and possess a high density of crystalline grain boundary defects.[13,21] The wet-chemistry method can effectively synthesize single-crystalline compounds and oxide-type magnetic NWs,[6,9] but the synthesis approach of (Fe, Co, Ni) metal NWs is still a challenge. Using the PVD approach, we have previously demonstrated the growth of free-standing single-crystalline nanowhiskers of varieties of different materials (copper, gold, and silver) on partially carbon-coated, oxidized Si (100), (110), and (111) substrates under molecular beam epitaxy (MBE) conditions.[19,20] In this report, we further explore the PVD scheme to synthesize the single-crystalline Fe and Co NWs.

The structural and magnetic properties of as-synthesized NWs can be examined via a range of micro-spectroscopy and magnetometry characterization tools.[23] Conventional x-ray diffraction and magnetometry measurements are usually carried out on a large number of NWs[2,3,10–12] and yield only averaged structural and magnetic information because of their relatively poor spatial resolution and limited sensitivity for nanosized samples. In contrast, the TEM techniques can provide a structural and compositional characterization of materials with atomic-scale resolution;[18,24,25] furthermore, imaging of magnetic domain walls is routinely performed on magnetic thin films by using the Lorentz-Transmission Electron Microscope (L-TEM).[26] However, Lorentz–Fresnel imaging has difficulty in studying the magnetic properties of some nanostructures due to existing Fresnel fringes of boundaries at the edge of NWs and no magnetic contrasts for the single magnetic domain. On the other hand, electron holography (EH) in the L-TEM has great potential for magnetic properties characterization,[17,27,28] and it can record the phase shift of high-energy electron waves that pass through samples in the nanometric spatial resolution, which directly reflects the magnetic and electrostatic potential in and around the specimen.[29] Some representative EH studies of magnetic nanostructures including various types of magnetic nanostructures have been reviewed.[30] The quantitative determination of nanoscale spin textures in 20-nm iron nanocubes[31] and the investigation of three-dimensional magnetic distribution of Co NWs[32] have also been reported. Thus, the TEM-based EH technique is now considered an ideal tool for studying the magnetic properties of nanosized materials at a single nanostructure level.[4,5,17]

In this study, we employ the PVD method to synthesize the high-quality Fe and Co NWs. Then, we use the Selected Area Electron Diffraction (SAED), the High-Resolution Transmission Electron Microscopy (HRTEM), and the energy-filtered imaging to characterize the structural and compositional properties of these ferromagnetic NWs in the atomic-scale resolution; furthermore, we study the magnetic properties of these NWs including the distribution of the magnetic field and their magnetic induction strength. These ferromagnetic NWs with a high aspect-ratio (tens of micrometers in length and tens of nanometers in diameter) are found to be single-crystalline without obvious planar defects and exhibit a magnetic single domain state.

EXPERIMENTAL

Sample preparation

Synthesis of Fe and Co NWs is carried out in an ultra-high vacuum (base pressure ~10^{-10} mbar)-MBE system (DCA Instruments, Finland). Ultra-pure Fe and Co are placed in crucibles located in effusion cells, heated via a filament. In order to activate the atom diffusion on the substrate surface, which is crucial for the nucleation and subsequent growth of the crystal whiskers, the substrate is heated to nearly 60% of the melting temperature (T_{Fe} = 800 °C, T_{Co} = 760 °C). In our case, the Fe and Co whiskers are grown directly on Mo wires (0.45 mm diameter) without any pretreatment.

Composition and structure property measurements

For TEM observations, Fe and Co NWs have been scratched off the Mo substrate and transferred to Cu-grids. The bright-field (BF) images and the corresponding SAED are performed on a TEM (JEM-ARM 200F) with spherical aberration correctors integrated into the image-forming system and the illumination system. The elemental mappings of these whiskers are measured on an Energy Dispersive X-ray (EDX) detector in the same TEM.

Electron holography characterization

Off-axis EHs are acquired in the Lorentz mode using an image-aberration-corrected microscope (FEI Titan 60–300), which is dedicated to EH and *in situ* magnetizing. This TEM operates with an ultrahigh-brightness field emission gun and is equipped with a wide pole piece gap. The gold coated thin electrostatic biprism (<1 μm) is located at the position of the selection area aperture and is electrostatically biased by hundreds of volts. Applying a suitable positive voltage (~100 V) to the biprism causes overlap between the objective wave and reference wave and results in the formation of the interference fringe pattern on the detector (the holographic interference fringe spacing is about 2.8 nm and the used sideband is 1/3 of the sideband to the center band and, as a result, the attainable spatial resolution is estimated to be ~8 nm).

In order to extract magnetic field distributions from the recorded phase shift, we use an *in situ* magnetizing process. To mitigate the phase artifacts introduced by electromagnetic lens distortions and biprism charging effects, we also record a reference hologram without the specimen under otherwise identical illumination conditions; in order to reduce the noises in the phase images, a cumulative acquisition approach is used to record 30 holograms with an exposure time of 2 s for each hologram. A set of custom-made Matlab codes is used to reconstruct phase images via the Fourier transform and band filter method and to align the multiple phase images via the cross correlation method prior to averaging the phase images for enhanced phase sensitivity. Moreover, to separate electric and magnetic phase contributions, pairs of phase images of reversed magnetization distributions were manually aligned and subtracted from one another.

RESULTS AND DISCUSSION

The morphology and crystal structure of the as-synthesized metal NWs are first examined by Scanning Electron Microscope (SEM) and TEM, respectively. Fe NWs sparsely grow on the Mo substrate by the observations of SEM [see Fig. 1(a)]. The Fe NWs exhibit variations in diameter (tens to hundreds of nm) and in length (a few to tens of micrometer), and upon close examination, most of them have whisker-like morphology with a sharp apex. Figure 1(b) shows a representative BF image of Fe NWs together with one of

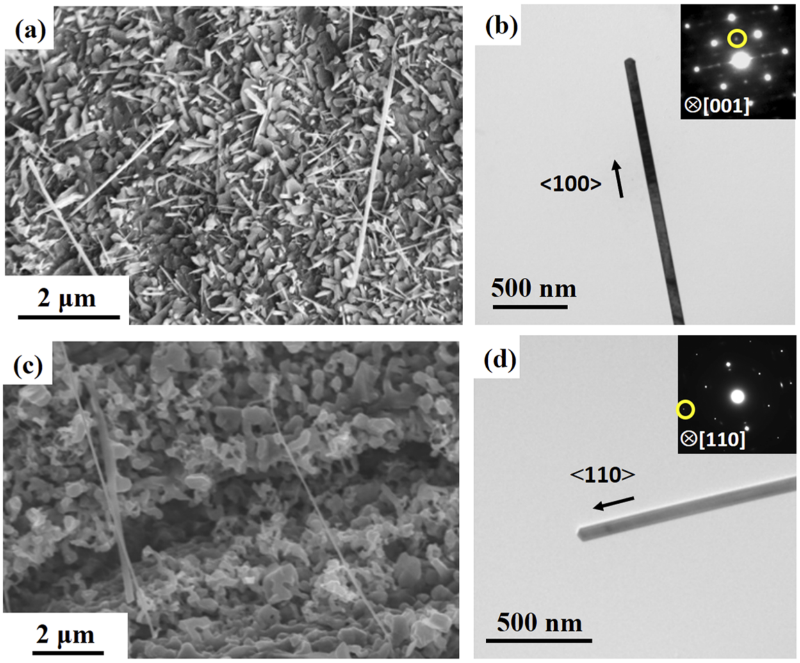

FIG. 1. (a) SEM micrograph and (b) TEM micrograph of as-synthesized Fe whiskers on Mo millimeter wire. Inset in (b) is the corresponding SAED pattern of the Fe NW and the yellow circle indicates (100) crystal plane of BCC α-Fe, suggesting the [100] preferential growth direction. (c) SEM micrograph and (d) TEM micrograph of as-synthesized Co whiskers on Mo millimeters wire. Inset in (d) is the corresponding SAED pattern of the Co NW and the yellow circle indicates the [110] direction of FCC β-Co crystal structure.

the corresponding SAED patterns as an inset. Several SAED patterns with sharp spots are taken along the nanowire (NW) axis revealing the single-crystalline nature of the NW without planar-type twinning or stacking fault defects. Furthermore, the SAED patterns of Fe NWs can be indexed with a body-centered cubic (BCC) structure (α-Fe),[33,34] and the preferential growth direction (axial direction) can be determined along the [100] crystallographic direction.[33]

Similar SEM and TEM measurements on the Co NWs are also carried out. Figure 1(c) shows a typical morphology of Co NWs grown on the Mo substrate. Note that in comparison to the growth of Fe NWs, the density of Co NWs is much less and the lengths of Co are apparently longer than those of Fe NWs. As for crystal structure observation, the BF images and corresponding SAED patterns of Co NWs reveal their single-crystalline nature without twinning defects or planar stacking faults [see Fig. 1(d)], which are similar to the results of Fe NWs; additionally, the crystal structure of Co NWs can be deemed a face-centered cubic (FCC) structure,[34] and their preferential growth direction is along the [110] crystallographic direction.[35]

It is well known that Fe and Co are prone to rapid oxidation upon exposure to ambient conditions, which makes them inappropriate for many applications. In the present study, although the Fe and Co NWs are produced in the ultra-high vacuum MBE chamber, the metal NWs are exposed to ambient conditions after removing from the MBE system. Thus, it is expected that the surface layers of Fe and Co NWs could be oxidized under ambient conditions. The High-Angle Annular Dark Field (HAADF) images of the Fe NW tip apex indicate that the thickness of Fe NW is uniform and there is a flat oxide shell covering the surface [see Fig. 2(a)]. To examine the extent of oxidation on these metal NWs, we performed the elemental mappings of Fe NWs based on the EDX characteristic spectroscopy in the Scanning Transmission Electron Microscopy (STEM) mode. According to the elemental distribution maps of iron [see Fig. 2(b)] and oxygen [see Fig. 2(b)] in one of the Fe NWs, one can see just the ~5 nm thick shell of oxide around the NWs.

Then, we carry out the HRTEM analysis on Fe NWs. The [100]-oriented Fe NW with a distinct contrast of the oxide shell is also reflected in the numerical fast Fourier transform (FFT) patterns of the shell and core regions [see Fig. 2(d)]. In the oxide shell region, a typical lattice spacing of ~0.83 nm is measured, which can be associated with the iron oxide of either Fe_3O_4[18] or Fe_2O_3.[25,36] A similar HRTEM analysis of Co NWs are also performed, and the lattice image of [110]-oriented Co NW is shown in Fig. 2(e). The oxide shell develops an epitaxial relation with the whisker core, which is evident from the presence of the moiré fringes. Two sets of spots are observed on the FFT pattern: one from the Co core (red circle) and the other from the oxide shell (yellow circle). Analysis of the FFT pattern reveals an epitaxial relationship between the oxide and the Co core as $(001)_{\text{oxide}} \| (001)_{\text{Co}}$ and $[100]_{\text{oxide}} \| [100]_{\text{Co}}$.[37] Note that some spots are due to the presence of the moiré (blue circle).

Taking together with the result of HRTEM, SAED, and EDX, we determine that the Fe NWs are covered with a thin but compact oxide shell. It is worth noting that these as-obtained NWs are examined after nearly two years of storage while the oxidation do not further develop, which is due to the compact passivation oxide shell covering the metal NWs against entire oxidation under ambient conditions.

In order to investigate the magnetic properties of these magnetic NWs, we map the magnetic field distributions of these NWs in the nanometric resolution by the off-axis EH technique. Figure 3(a) shows a schematic representation of the off-axis EH setup in the TEM. The holograms are recorded with the total phase shift

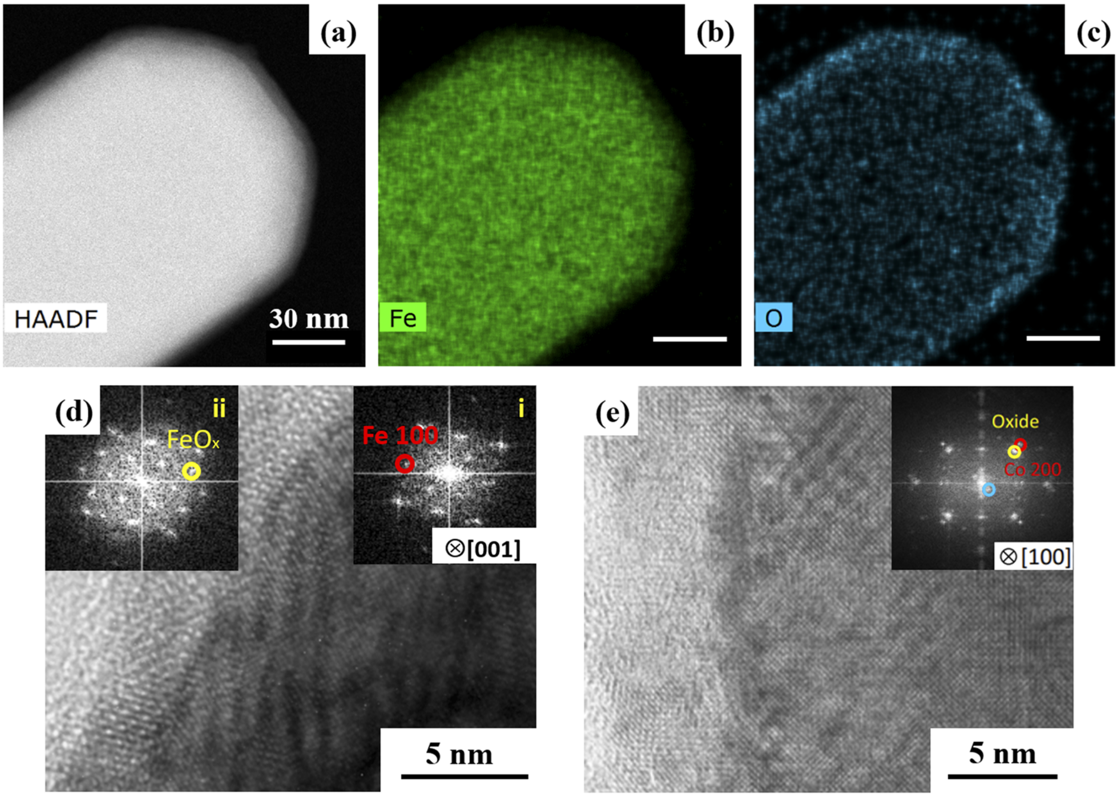

FIG. 2. (a) The HAADF image of Fe NWs tip apex. The elementary distribution of iron (b) and oxygen (c) in the Fe NWs tip apex. (d) The HRTEM image of Fe NWs viewed along the [001] zone axis. Inset (i) and (ii) are the FFT of Fe NWs core and Fe-oxide transitional area. (e) The HRTEM image of Co NWs viewed along [100] zone axis. Inset is the FFT pattern of Co NW core and Co-oxide transitional area.

in the specimen, including the electrostatic potential along with the in-plane magnetic potential, so we need to separate each term in the phase difference while studying the properties of ferromagnetic NWs by EH. To extract the magnetic potential contribution to the phase shift, the directions of magnetization in NWs are reversed *in situ* in TEM by tilting the sample ±75° and activating the conventional microscope objective lens to apply a magnetic field of about 1.5 T to the sample in the electron beam direction. The objective lens is then turned off and the sample tilts back to 0° for hologram acquisition in a zero-field condition with the specimen at remanence. After the *in situ* magnetizing process, the holograms are recorded with the specimen reversely magnetized. On the assumption that the *in situ* magnetizing process obtains a complete magnetization reversal because of the symmetric magnetic hysteresis loop of the magnetic NWs, compared with the flipping specimen method, the *in situ* magnetizing process eliminates the need of repetition of ex/insertion of the sample holder, making the magnetizing reversal experiments easier. Thus, the electrostatic potential contributions, mean inner potential (MIP), can be separated from the magnetic potential ones as described previously.[38] The difference in the reconstructed phase images [see Figs. 3(d) and 3(e)] of *in situ* magnetizing indicates that the magnetic potential in the two remanent states is completely reversed, so the electrostatic phase images are equal to the half of the summation of the two phases [see Fig. 3(f)] and the magnetic phase images are equal to the half of the subtraction between the two phases [see Fig. 3(g)].

To study the static magnetic structure of individual Fe NWs at remanence, one of the isolated Fe NWs with its apex part suspending on the Cu-grid is selected [see Fig. 4(a)]. The Fe NW is partly (~3 μm in length) suspended on the edge of the TEM grid making the apex part of the NW ideal specimen for off-axis EH measurements. Note that by tilting the NW and judging from the foreshortened image of tilted NW, we confirm that the end part of NW is lying flat on the Cu-grid. From the electrostatic phase image [see Fig. 3(f)], one can estimate the thickness variation in the specimen by assuming a single value of MIP for the specimen. According to the electrostatic phase shift formula,[30,39] $\Phi_E = C_E \cdot V_0 \cdot t$, where Φ_E is the electric phase shift and V_0 is an uniform assumption MIP of NWs and takes the value of 21 {±} 0.5 V. Because the value of MIP is 24 V for BCC Fe,[40,41] which is in excellent agreement with the calculated value of non-binding approximations based on the electron atomic scattering factors;[42] however, the surface of NWs is covered by compact oxide layers, whose MIP is about 12 V.[18,43] C_E is the electron interaction constant and takes the values of $6.53 * 10^{6}$ rad/V m[30] and t is the specimen thickness, and we determine that the cross section of this Fe NW is rectangular and the average thickness is about 55 nm, which has

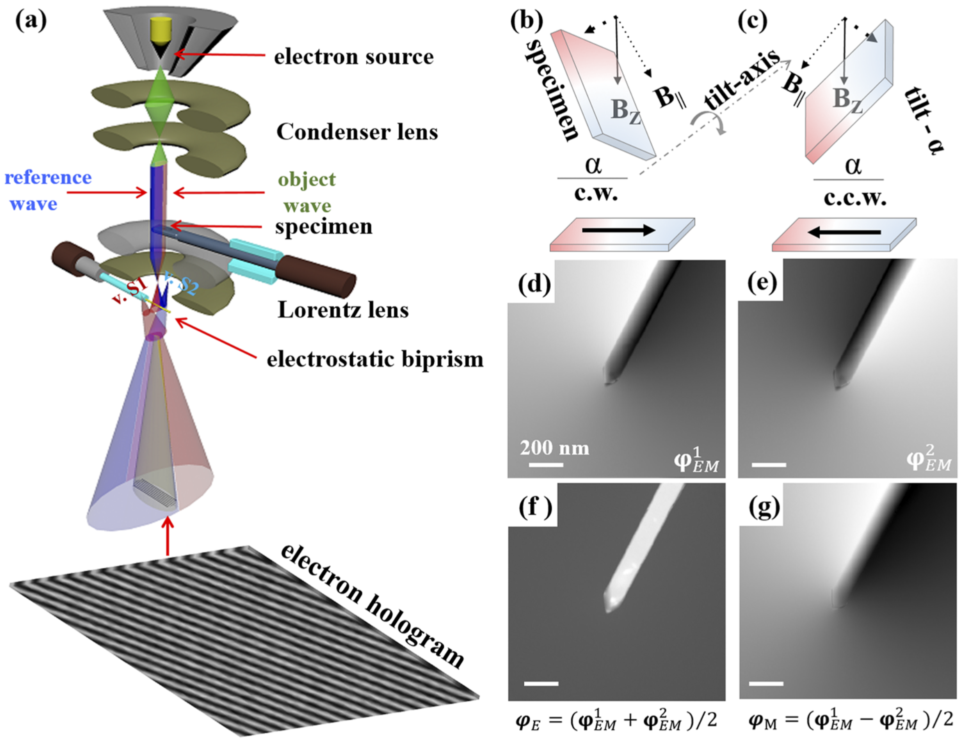

FIG. 3. (a) Schematic ray diagram of off-axis electron holography setup. [(b) and (c)] *In situ* magnetizing process involve the tilting of the specimen and the activating of the objective lens. [(d) and (e)] A pair of reconstructed total phase images with specimen reversely magnetized. (f) and (g) are the respective electric and magnetic phase images obtained from the simple calculation on total phase images of reversed magnetization in (d) and (e).

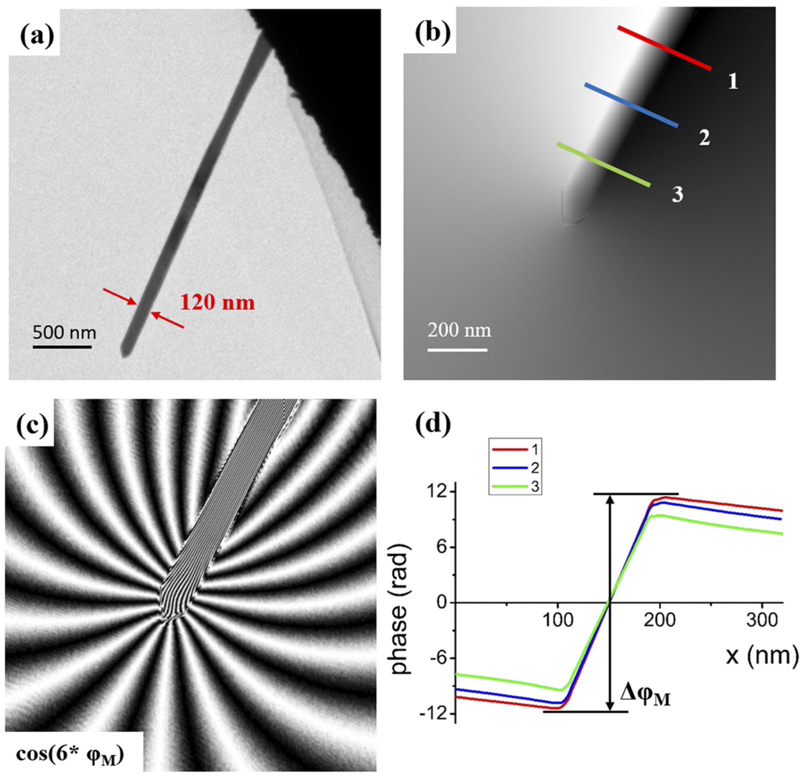

FIG. 4. (a) BF image of Fe NW on the Cu-grid. (b) Magnetic phase image of the apex part of Fe NW. Three lines (red, blue and green) mark the positions along the axis for phase profile extraction. (c) Equal-phase map constructed by a 6×-amplified original magnetic phase image, illustrating the projected in-plane magnetic induction field distributions inside and around the Fe NW. (d) Extracted phase profiles along the lines marked in (b).

been confirmed by the Electron Energy Loss Spectroscopy (EELS) log-ratio technique.

Figure 4(b) shows the magnetic phase map of the apex part of the Fe NW. In order to visualize the magnetic induction fields inside and around the magnetic the NW, we construct an equal-phase map by computing the cosine-function of the magnetic phase map; note that the value of magnetic phase shift is 6 times amplified before applying the cosine-function [see Fig. 4(c)]. Based on the equal-phase map, the stray field emanating from the tip of the Fe NW is clearly seen, while inside the NW, the equal-phase lines are too dense to be seen due to the strong induction fields inside the NW. The specific phase contrast that can be associated with the formation of the domain wall in the NW is not observed, suggesting that, at remanence, the Fe NW exhibits a uniformly magnetized state with its magnetization direction pointing along the NW axial direction. It should be noted that the reconstructed magnetic phase images may contain spurious phase impurities arising from stray fields and the phase reconstruction process.[43] In this work, in order to extract the projected in-plane magnetization distribution, we use a newly developed model-based magnetization reconstruction algorithm, by which the magnetization is iteratively reconstructed from the magnetic phase image recorded using electron holography (see the supplementary material). The uniformly magnetized state in NW allows one to estimate the magnetic induction by using the following formula:[6]

$$B = \frac{\hbar \Delta\Phi_M}{eS}, \tag{1}$$

where B is the magnetic flux density, $\hbar$ is the reduced Plank's constant, e is the electron charge, $\Delta\Phi_M$ is the magnetic phase shift across the NWs diameter, and S is the area of the cross section, provided that the stray fields outside NWs are negligibly weak or not contributing to the $\Delta\Phi_M$. However, due to the strong stray fields around the tip of NWs, one should avoid using the phase difference near the tip apex. Instead, the magnetic phase shift at the NWs positions further away from the tip can be used to measure the magnetic induction strength. Figure 4(d) plots the line profiles of the magnetic phase difference across the Fe NW in which the red, blue, and green profiles are measured at 600 nm, 400 nm, and 200 nm away from the NW apex, respectively, as marked in Fig. 4(b). The value of the green profile is obviously lower than other profiles, which indicates that the strong stray fields outside the NW have obviously affected the value of $\Delta\Phi_M$. In order to evaluate the magnetization by using the simple formula $\Delta\Phi_M \sim B * S$ relating the phase jump across the uniformly magnetized NW with cross section area, we select the phase profile at the position of the red line in Fig. 4(d). Then, we substitute the $\Delta\Phi_M$ across the diameter and the S of NW into Eq. (1), and the magnetic induction strength of Fe NW is measured to be 2.07 {±} 0.10 T, which is nearly equivalent to the theoretical calculation (2.20 T).[44–46] Note that the magnetic easy-axis of α-Fe is [100][46] and the axial direction of Fe NWs are also along the [100] crystallographic direction, hence making the Fe NWs stay in a single domain state at remanence after the *in situ* magnetizing process in the TEM. The 10% relative high measurement errors are taken from the phase sensitivity only, and it may become larger when

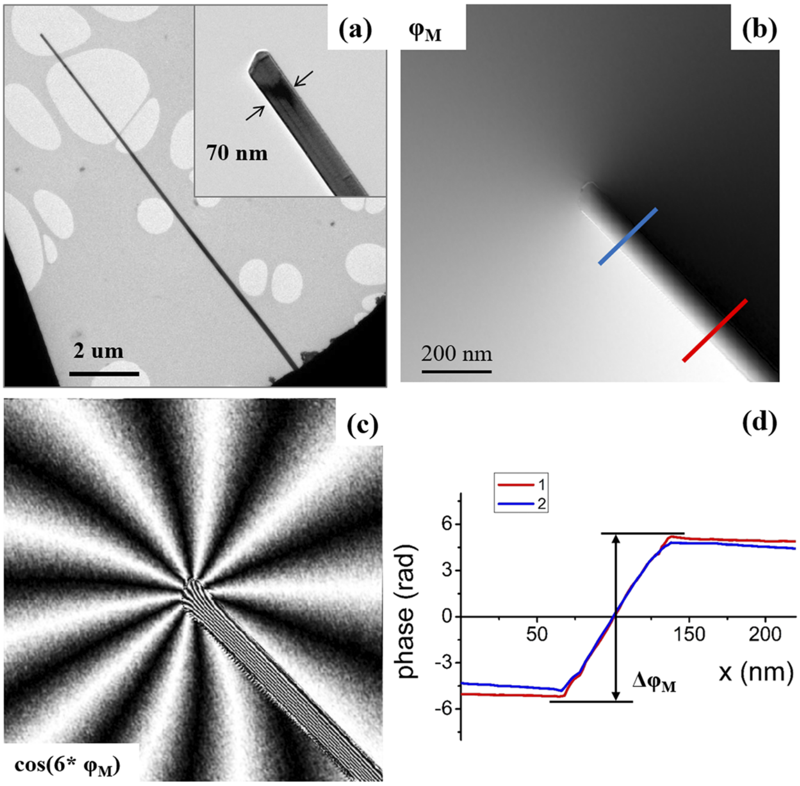

FIG. 5. (a) BF image of Co NW on the Cu-grid. Inset is the local amplified images of the apex of NW. (b) Magnetic phase image of the apex part of Co NW, in which the red and blue lines mark the positions along the axis for phase profile extraction. (c) Equal-phase map constructed by a 6×-amplified original magnetic phase image, illustrating the projected in-plane magnetic induction field distributions inside and around the Co NW. (d) Extracted phase profiles along the lines marked in (b).

considering other sources of error, particularly, the oxide surface layers on Fe NWs without well-known MIP and the stray field perturbation of the reference wave could lead to measurement errors of NWs thickness.

The magnetic properties of Co NWs also have been investigated using similar off-axis EH experiments. A typical and suitable Co NW is selected for the EH measurement, whose length is more than 12 μm and the diameter is about 70 nm [see Fig. 5(a)]. The electrostatic and magnetic potential phase images are obtained by the above-mentioned *in situ* magnetizing process and phase separation method. In the magnetic phase image of the apex part of Co NW, the blue and red lines mark the positions of magnetic phase profiles at 200 nm and 500 nm away from the apex, respectively [see Fig. 5(b)]. To obviously illustrate the projected magnetic induction field of the apex part of Co NW, an equal-phase map is constructed in the form of a cosine-function based on the 6 times amplified magnetic phase [see Fig. 5(c)] in which the white–black contrast map represents the projected induction field lines. It is similar to the case of Fe NWs, and the emanating stray field lines outside the apex and the field lines inside NWs suggest that the Co NW is also uniformly magnetized along the axial direction. Due to the higher aspect-ratio of Co NWs, the values of magnetic phase different in both marked positions are nearly the same [see Fig. 5(d)]. This indicates that the stray fields outside Co NWs are more divergent than Fe NWs and the stray fields adjacent to Co NWs are relatively weak. We select the phase profile located at 500 nm for the measurement of $\Delta\Phi_M$; moreover, the cross section of Co NW is nearly circular, and the area of cross section is calculated based on the electrostatic phase shift formula.[30,39] According to Eq. (1), the value of magnetic induction strength of Co NW is 1.83 {±} 0.15 T, which is in good agreement with the theoretical value (1.88 T).[46] However, due to the Co NW with a high aspect-ratio (tens of micrometer in length vs tens of nanometer in diameter), the shape anisotropy of Co NWs dominates the magnetocrystalline anisotropy of β-Co with its weak easy-axis along the [111] direction.[47] Consequently, the magnetization direction of Co NWs is along the axial direction with the [110] crystallographic direction.

We note that we also conducted a synthesis of Ni NWs and the magnetic measurement by EH. However, the Ni NWs are in the form of polycrystalline consisting of grains, and the resultant magnetic phase image is of low quality. Further optimization of synthesis for single-crystalline Ni NWs is still in progress.

CONCLUSION

In summary, we have successfully synthesized high-quality Fe and Co NWs via the PVD method in the MBE system. Then, we used a range of TEM techniques to study the crystallinity and composition of these metal NWs. The BF images and SAEDs reveal the single-crystalline nature of these NWs; moreover, the surface of all NWs is covered by the thin but compact passivation layers of oxides that prevent their further oxidation under ambient conditions, as revealed by the elemental mappings and HRTEM images. To quantify the magnetic properties of Fe and Co NWs, we perform the *in situ* magnetizing process and off-axis EH measurement to obtain the magnetic induction field distributions of Fe and Co NWs. The analyses of the EH experiment reveal that these ferromagnetic NWs are uniformly magnetized along the axis direction, and the measured magnetic induction strengths are 2.07 {±} 0.10 T for Fe NWs and 1.83 {±} 0.15 T for Co NWs, which are very close to the respective theoretical values. Our results provide a route to synthesizing metal ferromagnetic NWs and exemplifying the magnetic quantification of nanomaterials at a single nanostructure level.

SUPPLEMENTARY MATERIAL

See the supplementary material for (1) the magnetic phase images of the original, the corrected one after removal of linear phase ramps, and the reconstructed one generated from the reconstructed magnetization, (2) the extent of thickness variations, and (3) the reconstructed projected magnetization distributions of the Fe and Co NWs.

ACKNOWLEDGMENTS

This work was supported by the National Key Research and Development Program of China (Grant No. 2017YFA0303000), the National Natural Science Foundation of China (Grant Nos. 11974019, 11447703, and 61574017), and the Graduate Technological Innovation Project of Beijing Institute of Technology (Grant No. 2018CX20029). Z.-A.L. acknowledges the Hundred Talent Program (B) of the Chinese Academy of Sciences.

REFERENCES

[1] N. Biziere, C. Gatel, R. Lassalle-Balier, M. C. Clochard, J. E. Wegrowe, and E. Snoeck, Nano Lett. **13**, 2053 (2013).

[2] K. Soulantica, F. Wetz, J. Maynadié, A. Falqui, R. P. Tan, T. Blon, B. Chaudret, and M. Respaud, Appl. Phys. Lett. **95**, 152504 (2009).

[3] X. Zhang, X. Jiang, F. Xiong, C. Wang, and S. Yang, Mater. Res. Bull. **95**, 248 (2017).

[4] G. L. Drisko, C. Gatel, P.-F. Fazzini, A. Ibarra, S. Mourdikoudis, V. Bley, K. Fajerwerg, P. Fau, and M. Kahn, Nano Lett. **18**, 1733 (2018).

[5] P. Simon, D. Wolf, C. Wang, A. A. Levin, A. Lubk, S. Sturm, H. Lichte, G. H. Fecher, and C. Felser, Nano Lett. **16**, 114 (2016).

[6] J. Zhang, S. Zhu, H. Li, L. Zhu, Y. Hu, W. Xia, X. Zhang, Y. Peng, and J. Fu, Nanoscale **10**, 10123 (2018).

[7] G. Yang, J. Tang, S. Kato, Q. Zhang, L. C. Qin, M. Woodson, J. Liu, J. W. Kim, P. T. Littlehei, C. Park, and O. Zhou, Appl. Phys. Lett. **87**, 123507 (2005).

[8] M. R. Koblischka and U. Hartmann, Ultramicroscopy **97**, 103 (2003).

[9] K. A. Atmane, C. Michel, J.-Y. Piquemal, P. Sautet, P. Beaunier, M. Giraud, M. Sicard, S. Nowak, R. Losnoe, and G. Viau, Nanoscale **6**, 2682 (2014).

[10] N. Cordente, M. Respaud, C. Amiens, F. Senocq, M.-J. Casanove, and B. Chaudret, Nano Lett. **1**, 565 (2001).

[11] J. Bao, C. Tie, and Z. Xu, Adv. Mater. **13**, 1631 (2001).

[12] K. V. Frolov, D. L. Zagorskii, I. S. Lyubutin, M. A. Chuev, I. V. Perunov, S. A. Bedin, A. A. Lomov, V. V. Artemov, and S. N. Sulyanov, JETP Lett. **105**, 319 (2017).

[13] H. Pan, B. Liu, J. Yi, C. Poh, S. Lim, J. Ding, Y. Feng, C. H. A. Huan, and J. Lin, J. Phys. Chem. B **109**, 3094 (2005).

[14] N. Bagkar, K. Seo, H. Yoon, J. In, Y. Jo, and B. Kim, Chem. Mater. **22**, 1831 (2010).

[15] S.-i. Kim, H. Yoon, K. Seo, Y. Yoo, S. Lee, and B. Kim, ACS Nano **6**, 8652 (2012).

[16] K. T. Chan, J. J. Kan, C. Doran, L. Ouyang, D. J. Smith, and E. E. Fullerton, Nano Lett. **10**, 5070 (2010).

[17] N. Mathur, M. J. Stolt, K. Niitsu, X. Yu, D. Shindo, Y. Tokura, and S. Jin, ACS Nano **13**, 7833 (2019).

[18] M. Chang, L. Chou, C. Hsieh, Y. Chueh, Z. Wang, Y. Murakami, and D. Shindo, Adv. Mater. **19**, 2290 (2007).

[19] W. Huang, V. Srot, J. Wagner, and G. Richter, Mater. Des. **182**, 108098 (2019).

[20] G. Richter, K. Hillerich, D. S. Gianola, R. Monig, O. Kraft, and C. A. Volkert, Nano Lett. **9**, 3048 (2009).

[21] A. Fernandez-Pacheco, J. M. D. Teresa, R. Cordoba, and M. R. Ibarra, J. Phys. D: Appl. Phys. **42**, 055005 (2009).

[22] A. Fernandez-Pacheco, L. Serrano-Ramon, J. M. Michalik, M. R. Ibarra, J. M. De Teresa, L. O'Brien, D. Petit, J. Lee, and R. P. Cowburn, Sci. Rep. **3**, 1492 (2013).

[23] H. Hopster and H. P. Oepen, *Magnetic Microscopy of Nanostructures* (Springer, Hamburg, Germany, 2005), Vol. 13.

[24] D. B. Williams and C. B. Carter, *Transmission Electron Microscopy* (Springer, New York, USA, 2009), Vol. 4.

[25] Y. L. Chueh, M. W. Lai, J. Q. Liang, L. J. Chou, and Z. L. Wang, Adv. Funct. Mater. **16**, 2243 (2006).

[26] M. Schneider, H. Hoffmann, and J. Zweck, Appl. Phys. Lett. **77**, 2909 (2000).

[27] C. T. Koch and A. Lubk, Ultramicroscopy **110**, 460 (2010).

[28] R. C. Che, M. Takeguchi, M. Shimojo, W. Zhang, and K. Furuya, Appl. Phys. Lett. **87**, 223109 (2005).

[29] H. Lichte and M. Lehmann, Rep. Prog. Phys. **71**, 016102 (2008).

[30] R. E. Dunin-Borkowski, T. Kasama, and R. J. Harrison, "Electron holography of nanostructured materials," in *Nanocharacterisation* (Royal Society of Chemistry, 2007), pp. 138–183.

[31] E. Snoeck, C. Gatel, L. M. Lacroix, T. Blon, S. Lachaize, J. Carrey, M. Respaud, and B. Chaudret, Nano Lett. **8**, 4293 (2008).

[32] D. Wolf, L. A. Rodriguez, A. Béché, E. Javon, L. Serrano, C. Magen, C. Gatel, A. Lubk, H. Lichte, S. Bals, G. V. Tendeloo, A. Fernández-Pacheco, J. M. D. Teresa, and E. Snoeck, Chem. Mater. **27**, 6771 (2015).

[33] T. Fujita, M. Chen, X. Wang, B. Xu, K. Inoke, and K. Yamamoto, J. Appl. Phys. **101**, 014323 (2007).

[34] G. Y. Guo and H. H. Wang, Chin. J. Phys. **38**, 949 (2000).

[35] G. Tourillon, L. Pontonnier, J. P. Levy, and V. Langlais, Electrochem. Solid State Lett. **3**, 20 (1999).

[36] S. Brice-Profetaa, M.-A. Arrioa, E. Troncb, N. Menguya, I. Letarda, C. C. d. Moulinc, M. Noguese, C. Chaneacb, J.-P. Jolivetb, and P. Sainctavi, J. Magn. Magn. Mater. **288**, 354 (2005).

[37] G. Dumpich, T. P. Krome, and B. Hausmanns, J. Magn. Magn. Mater. **248**, 241 (2002).

[38] R. E. Dunin-Borkowski, M. R. McCartney, D. J. Smith, and S. S. P. Parkin, Ultramicroscopy **74**, 61 (1998).

[39] L. Li, D. J. Smith, E. Dailey, P. Madras, J. Drucker, and M. R. McCartney, Nano Lett. **11**, 493 (2011).

[40] A. Sanchez and M. A. Ochando, J. Phys. C: Solid State Phys. **18**, 33 (1985).

[41] V. Edgar, F. A. Lawrence, and C. J. David, *Introduction to Electron Holography* (University of Tennessee, Tennessee, 1999), Vol. 12.

[42] L. M. Peng, G. Ren, S. L. Dudarev, and M. J. Whelan, Acta Crystallogr., Sect. A: Found. Crystallogr. **52**, 257 (1996).

[43] S. Sturm, M. Siglreitmeier, D. Wolf, K. Vogel, M. Gratz, D. Faivre, A. Lubk, B. Büchner, E. V. Sturm, and H. Cölfen, Adv. Funct. Mater. **29**, 1905996 (2019).

[44] V. L. Moruzzi, J. F. Janak, and A. R. Williams, *Calculated Electronic Properties of Metal* (Pergamon, New York, 1978).

[45] J. Küeler, Phys. Lett. **81**, 81 (1980).

[46] R. C. O'Handley, *Modern Magnetic Materials* (Wiley-lnterscience, 2000), Vol. 17.

[47] M. Jamet, W. Wernsdorfer, C. Thirion, D. Mailly, V. Dupuis, P. Melinon, and A. Perez, Phys. Rev. Lett. **86**, 4676 (2001).